

Development of a flat calibration unit for accurate flat fielding in the mid-infrared region

Akira C. Naruse,^{a,*} Takafumi Kamizuka^{b,a}, Takashi Miyata^{b,a,b,c},
Shigeyuki Sako,^{a,b,c} Ryou Ohsawa^{b,d}, Kentaro Asano,^a Atsushi Nishimura^{b,e},
Itsuki Sakon^{b,f}, Kengo Tachibana,^a and Hirokazu Iida^a

^aThe University of Tokyo, Graduate School of Science, Institute of Astronomy, Tokyo, Japan

^bThe University of Tokyo, UTokyo Organization for Planetary Space Science, Tokyo, Japan

^cThe University of Tokyo, Collaborative Research Organization for Space Science and Technology, Tokyo, Japan

^dNational Astronomical Observatory of Japan, Tokyo, Japan

^eNational Astronomical Observatory of Japan, Nobeyama Radio Observatory, Nagano, Japan

^fThe University of Tokyo, Graduate School of Science, Department of Astronomy, Tokyo, Japan

ABSTRACT. Time-domain astronomy is important in the field of modern astronomy, and monitoring observations in the mid-infrared region with 1% photometric accuracy to study the variables and transients is becoming essential. The non-uniformity of the sensitivity caused by the optical characteristics of instruments and differences in the response curves of individual detector pixels degrade photometric accuracy. Therefore, to achieve 1% photometric accuracy, a flat-field correction for the non-uniformity with an accuracy of better than 1% is required. We developed a flat calibration unit (FCU) consisting of a silicon lens, a blackbody source, and two flat folding mirrors. We conducted proof-of-concept tests of the FCU by measuring the accuracy and stability of flat frames obtained using the FCU. The accuracies of the flat frames were 0.23% at 7.7 μm , 0.43% at 9.6 μm , 0.34% at 11.5 μm , and 0.84% at 20.9 μm , which are sufficient to achieve 1% photometric accuracy. The flat frames obtained using the FCU were stable over a period of 29 h within the accuracies of 0.13% at 7.7 μm , 0.12% at 9.6 μm , 0.22% at 11.5 μm , and 0.52% at 20.9 μm , indicating that it is sufficient to obtain flat frames once per night.

© The Authors. Published by SPIE under a Creative Commons Attribution 4.0 International License. Distribution or reproduction of this work in whole or in part requires full attribution of the original publication, including its DOI. [DOI: [10.1117/1.JATIS.9.3.038004](https://doi.org/10.1117/1.JATIS.9.3.038004)]

Keywords: calibration system; flat fielding; mid-infrared; University of Tokyo Atacama Observatory; MIMIZUKU

Paper 23021G received Feb. 14, 2023; revised Jun. 30, 2023; accepted Jul. 28, 2023; published Aug. 11, 2023.

1 Introduction

Time-domain astronomy is important in the field of modern astronomy. It provides us with features of the dynamic universe, which were previously not possible to obtain through conventional snapshot observations. In recent years, optical and near-infrared monitoring photometries have been conducted to study the variables and transients, such as late-type stars, young stellar objects, supernovae, active galactic nuclei, and exoplanets. In the first successful transit observation of an exoplanet, a dimming of 2% was detected in the *R* band with a photometric accuracy of better than 1%.¹ Following this, considerably more accurate monitoring observations have been made to study the exoplanets, such as in the Kepler mission² and the Transiting Exoplanet Survey Satellite mission.³

*Address all correspondence to Akira C. Naruse, naruse-akira151@g.ecc.u-tokyo.ac.jp

Objects showing significant transient variations in the mid-infrared (MIR: 3 to 40 μm) region have been discovered in recent years. MIR variations of main sequence stars with debris disks are interesting phenomena. They have been discussed as a possible dust enrichment owing to planetary-scale collisions. One example is BD +20 307. Its flux within the range of 8.8 to 12.5 μm has increased by 10% over 9 years,⁴ suggesting an average increase in the rate of $\sim 1\%$ per year. MIR monitoring observations with an accuracy in the order of 1% are highly required for further observational studies of these transient phenomena.

Both ground- and space-based telescopes are useful for monitoring infrared transients. Focusing on ground-based observations, differential photometry with multiple objects allows us to rectify the time variations in apparent fluxes due to the fluctuation of atmospheric absorption. However, in ground-based MIR observations, low sensitivity due to the high background radiation often makes it difficult to observe a sufficient number of stable references within the same field of view simultaneously. Empirically, $\sim 10\%$ accuracy has been achieved in conventional MIR observations, wherein the target and reference images are obtained alternately.

To achieve high-precision long-term monitoring and rapid follow-up observations in the MIR region, we developed an MIR imager and spectrograph MIMIZUKU^{5–10} for the University of Tokyo Atacama Observatory (TAO) 6.5-m telescope.^{11–15} MIMIZUKU has an optomechanical unit named Field Stacker (FS)¹⁶ with two pick-off mirrors and a combining mirror, which enables simultaneous observations of two different sky regions. We aim to achieve MIR monitoring observations with a photometric accuracy of 1% by simultaneously observing the target and reference objects using the FS.

To achieve an MIR photometric accuracy of 1%, we require the correction of the non-uniformity of the sensitivity with an accuracy of better than 1% as well as differential photometry. Such correction is also effective when observing diffuse objects spread over multiple pixels, such as nebulae and planets. The non-uniformity of the sensitivity is caused by the optical characteristics of instruments and differences in the response curves of individual detector pixels and is generally corrected through flat fielding. Object frames are divided by flat frames obtained by irradiating the detector with a uniform surface light source.

When the detector pixels have non-linear responses to the number of detected photons, as shown in Fig. 1, careful handling of the flat-field correction is required. In ground-based MIR observations, we use a narrow range of the detector well owing to high background radiation. Therefore, the local gradient of the response curve is more important rather than the global gradient. In the self-sky flat method used as a standard reduction procedure for Subaru/COMICS data,¹⁷ flat frames are created from blank sky images, and object frames are corrected using the global gradient. In such cases, the global gradient method overestimates the gradients in the operating range of the detector well, as shown in Fig. 1(a).

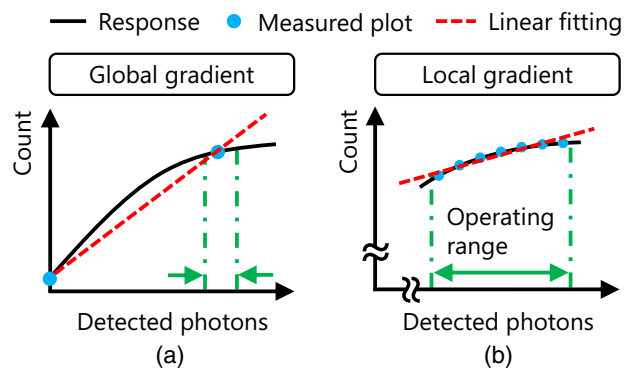


Fig. 1 Conceptual diagram of flat fielding using (a) the global and (b) local gradients. The black solid curves represent the response curves of a pixel. The blue points represent the measurement points, and the red dashed lines represent linear fits to derive the gradients. The typical flux level in observations is shown as the operating range by the green dashed and dotted lines. The operating range is enlarged in panel (b). The gradients are estimated using the vertical intercept and another measured sample in the global gradient method, whereas multiple points within the operating range are used in the local gradient method. The local gradient yields a more appropriate fit in the operating range than the global gradient.

It is preferable to derive the sensitivity curve or simply estimate the local gradients around the operating range by considering multiple measurement points within the operating range, as shown in Fig. 1(b). There are two previous studies on flat-fielding methods for the local gradient in the literature. One study utilized the flux difference of the sky background at different airmasses.^{18,19} This method works in the Q band but is considered unsuitable in the N band because the radiation from the telescope is higher than that of the sky background and the count level is almost independent of the airmass at observation sites with low precipitable water vapor. The other study utilized the variability of atmospheric radiation.²⁰ However, we can apply this method only when the observation condition is unstable, and the atmospheric radiation is highly time-varying.

From the above discussion, the following three design requirements are noted, which are necessary for accurate flat fielding in ground-based MIR observations: (1) all detector pixels must be uniformly irradiated; (2) multiple measurement points must be sampled in the operating range; and (3) flat fielding must be performed independently of atmospheric conditions. In this study, we developed a flat calibration unit (FCU) that satisfies these three requirements. The remainder of this paper is organized as follows: the detailed design of the FCU is explained in Sec. 2. The experimental procedure and the data analysis method of proof-of-concept tests of the FCU are presented in Sec. 3. We report the results of the evaluation in Sec. 4 and discuss these results in Sec. 5. The concluding points are summarized in Sec. 6.

2 Design

The cold optics of MIMIZUKU is installed inside a chamber fixed to a $2\text{ m} \times 2\text{ m} \times 2\text{ m}$ framework. The FS is located inside a cylinder, which is mounted on the chamber and has a diameter of 1.1 m and a height of 90 mm. The FCU is designed to be installed inside this cylinder. A 43-mm square focal plane with an F -number of 12.2 is formed at 22 mm above the bottom center of the cylinder. We designed the FCU to enable flat fielding across the entire focal plane.

Figure 2 shows the design and photograph of the FCU. The FCU consists of a silicon lens, a blackbody source, and two flat folding mirrors. The focal length of the lens is 210 mm, and its effective diameter is 80 mm. The blackbody we adopted was IRC 150 manufactured by Advanced Energy, which has the following specifications: effective emissivity of 0.98 ± 0.004 , temperature reproducibility of 0.2 K, temperature stability of 0.1 K, and surface temperature uniformity of 0.2 K (the latter three characteristics represent peak-to-valley measurements). Its physical diameter is 50.8 mm, and we used its central region with a diameter of 18 mm. These components were placed in front of the MIMIZUKU entrance window. The radiation from the blackbody source goes through the lens reflected by the two folding mirrors to reach the MIMIZUKU cold optics. The optical position of the blackbody is conjugate to the instrument pupil. As the FCU is retractable, we can quickly switch between the observation and calibration modes.

The FCU proposed in this study satisfied the three requirements described in Sec. 1: (1) the detector was irradiated uniformly because the blackbody source was placed at the optical pupil,

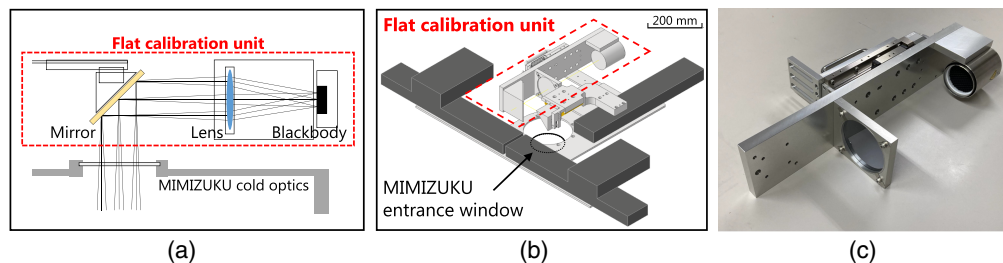


Fig. 2 (a) Conceptual diagram of the FCU. The FCU is placed above the MIMIZUKU cold optics. The blackbody placed at the optical pupil irradiates the detector uniformly. Although only one mirror is depicted in the conceptual diagram, two folding mirrors are used to introduce light to the MIMIZUKU cold optics. (b) Three-dimensional drawing of the FCU placed at the FS system. The FCU is encircled by the red dashed line, and the remaining components belong to the FS system. (c) Real picture of the FCU.

which means that all pixels of the detector see the same blackbody region as a result of perfect defocusing, and a diffuser is not necessarily required; (2) multiple measurement points were taken from the operating range because the radiation flux on the detector was changeable by varying the temperature of the blackbody source; and (3) flat fielding was performed independently of atmospheric conditions because the blackbody was used as the light source instead of the sky background. The thermal radiation from the FCU or the entrance window degrades the uniformity of the light source. However, this was eliminated by extracting only the variable component of the blackbody radiation that changes with the blackbody temperature.

To achieve a flat-fielding accuracy of better than 1%, it is necessary to irradiate the detector with a uniformity sufficiently better than 1%. All pixels of the detector received radiation from the same blackbody region because the blackbody source was placed at the optical pupil. However, each pixel received blackbody radiation emitted at a different exit angle. Therefore, the exit-angle dependence of the blackbody radiation was investigated. The maximum exit angle of the radiation reaching the detector θ_{\max} is given by

$$\theta_{\max} = \arctan\left(\frac{\phi_{\text{lens}} - \phi_{\text{bb}}}{2f}\right), \quad (1)$$

where ϕ_{lens} is the effective diameter of the lens, ϕ_{bb} is the diameter of the used region of the blackbody, and f is the focal length of the lens. By substituting $\phi_{\text{lens}} = 80$ mm, $\phi_{\text{bb}} = 18$ mm, and $f = 210$ mm, we obtained $\theta_{\max} = 8.4$ deg. Our test of the blackbody source demonstrated an angular dependence of $<0.03\%$ in the range of ± 10 deg, which is much better than 1%. Therefore, the blackbody we adopted meets the requirement of the FCU.

3 Experiments and Data Analysis

In conventional ground-based MIR observations, flat fielding was conducted using the self-sky flat,¹⁷ airmass differences,^{18,19} or atmospheric variations²⁰ instead of employing dedicated units, such as the FCU. We conducted proof-of-concept tests of our technique by measuring the accuracy and stability of the flat frames obtained using the FCU (FCU flat frames). We used the Aquarius Si:As $1\text{k} \times 1\text{k}$ detector installed in the MIMIZUKU MIR-S channel and four imaging filters with central wavelengths of 7.7, 9.6, 11.5, and 20.9 μm . Table 1 presents the properties of the filters.

Initially, we created flat frames using the FCU. The FCU was placed vertically along the optical axis of the instrument without using the folding mirrors, as shown in Fig. 3(a). The data were acquired by varying the temperature of the blackbody; eventually, flat frames were obtained (Sec. 3.1). Flat frames simulating the self-sky flat frames (conventional flat frames) were created for a comparison with the FCU flat frames (Sec. 3.2). To evaluate the accuracy of the flat frames, we obtained images of the blackbody itself as reference data for uniform images, as shown in Fig. 3(b) (Sec. 3.3). The reference images divided by the FCU flat frames would ideally be flat. However, residual patterns created by the absorption and reflection of the silicon lens appeared in these images; therefore, they were corrected (Appendix A). Finally, the flatness of the flat-fielded images was evaluated (Sec. 3.4). Figure 4 shows a flowchart outlining the above procedure. Furthermore, we investigated the temporal instability of the FCU flat frames by monitoring them for ~ 29 h (Sec. 3.5).

Table 1 Central wavelength, the FWHM of the transmission band, and the average transmittance of each imaging filter corresponding to the filter name.

Filter name	Central wavelength (μm)	FWHM (μm)	Average transmittance (%)
7.7 μm	7.67	0.211	84
9.6 μm	9.61	0.958	91
11.5 μm	11.5	1.02	86
20.9 μm	20.9	1.78	78

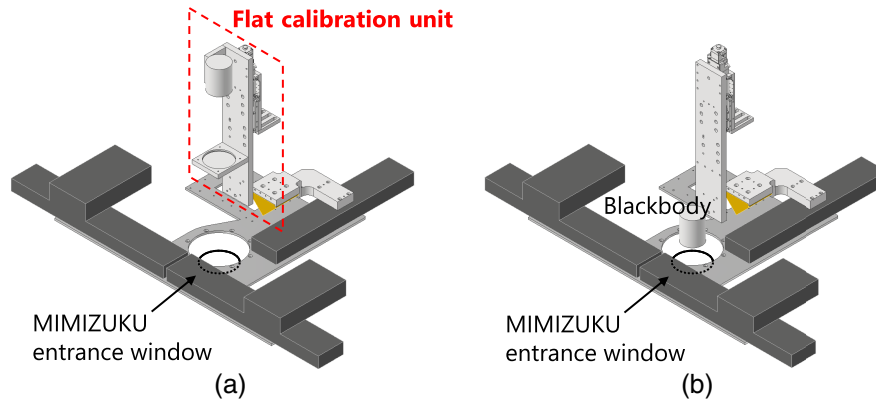


Fig. 3 (a) Setup for obtaining flat frames using the FCU. The FCU was vertically placed along the optical axis of the instrument without using the folding mirrors. (b) Setup for acquiring reference images to evaluate the accuracy of flat frames. The FCU was removed, and the blackbody was placed on the focal plane. In both setups, the MIMIZUKU cold optics were located under the entrance window.

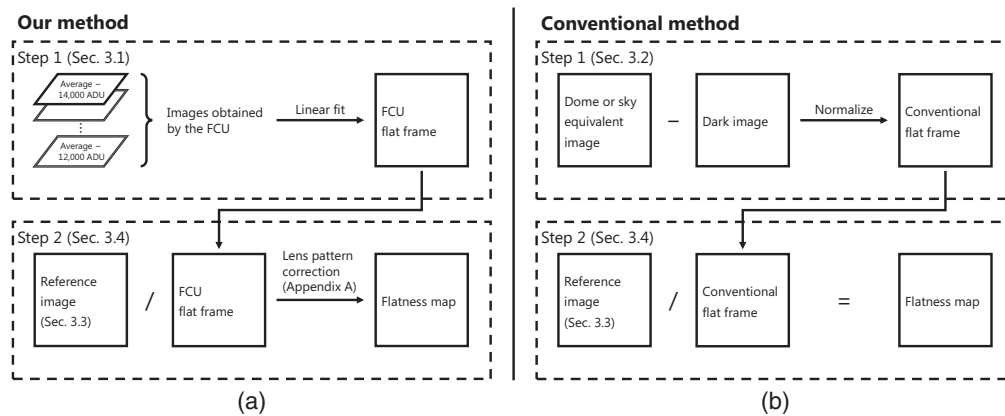


Fig. 4 Flowchart for creating the flatness maps of (a) the FCU flat-fielded images and (b) those of the conventional flat-fielded images. The reference images were obtained by normalizing the blackbody images with a high-count level minus those with a low-count level. The flatness maps of the FCU flat-fielded images were derived by dividing the reference images by the FCU flat frames and correcting the absorption and reflection of the silicon lens. The flatness maps of the conventional flat-fielded images were created by dividing the reference images by the conventional flat frames.

3.1 Creating the FCU Flat Frames

Flat frames were obtained using the FCU. The blackbody was heated to 150°C, and exposures were made to obtain data. The exposure time was adjusted for each filter such that the count level reached $\sim 14,000$ ADU. This simulated actual MIMIZUKU observations, that is, we typically utilize a count range of $\sim 12,000$ to 14,000 ADU, which is sufficiently lower than the saturation limit and aimed at reaching the sky background limit.²⁰ The blackbody was then turned off. While the temperature of the blackbody decreased, the data were continuously acquired. The above operation was repeated until the total number of acquired frames reached 100. For each pixel of the detector, the count of the pixel was plotted against the average count of all pixels in the photosensitive region, and the gradient was derived using the least-squares method. Normalization was performed such that the averages of the gradients for all pixels in the photosensitive region were in unity. The resulting gradients were the values of each pixel of the flat frames (flat values). To reduce the random noise, the resulting flat frames were stacked.

In the derivation process of the gradients, the non-uniform thermal radiation was eliminated. The light incident on the detector consists of two components: F_{thermal} , which is the non-uniform thermal emission from the FCU and entrance window constant in time, and $F_{\text{bb}}(T)$, which is the

uniform blackbody radiation dependent on the temperature of the blackbody. When deriving the gradient, we extracted the variable component of $F_{\text{bb}}(T)$ and excluded the effect of F_{thermal} by taking the difference of the images obtained while changing the temperature of the blackbody source. That is,

$$[F_{\text{thermal}} + F_{\text{bb}}(T_1)] - [F_{\text{thermal}} + F_{\text{bb}}(T_2)] = F_{\text{bb}}(T_1) - F_{\text{bb}}(T_2) \quad (T_1 \neq T_2). \quad (2)$$

3.2 Creating the Conventional Flat Frames

The comparison of the FCU flat frames and the flat frames obtained using conventional methods, such as the self-sky method, is informative. We obtained images of the ceiling of the laboratory instead of the sky and created flat frames using the same process as the self-sky method, that is, we created flat frames by subtracting dark images from ceiling images and normalized them such that the average counts of all pixels in the photosensitive region were unity. When taking ceiling images, the exposure time was adjusted for each filter such that the count level reached $\sim 14,000$ ADU.

3.3 Creating the Reference Images

To measure the accuracy of flat frames, we acquired images of the blackbody placed at the instrument focus. Two types of images were obtained: high-count images with an average count of $\sim 14,000$ ADU and low-count images with an average count of $\sim 12,000$ ADU. Dark frames were subtracted from both types of images, and we used the normalized differential images of these two images as the reference images. Normalization was performed such that the average counts of all pixels were in unity. Using differential images is effective for eliminating unwanted radiation from the window and other ambient regions. This also provides a good simulation of the actual observations, as mentioned in Sec. 3.1. To reduce the random noise, 1200 frames were stacked for the blackbody images with low-count levels, those with high-count levels, and dark images.

3.4 Evaluation of the Flatness of the Flat-Fielded Images

The reference images derived in Sec. 3.3 were divided by the FCU flat frames derived in Sec. 3.1 or the conventional flat frames derived in Sec. 3.2. The correction for the absorption and reflection of the lens described in Appendix A was conducted for the former. The resulting images are referred to as “flatness maps of the FCU flat-fielded images” or “flatness maps of the conventional flat-fielded images,” respectively. Assuming that the reference images are perfectly uniform, the deviation of the counts from the unity in these images represents the accuracy of flat frames.

3.5 Temporal Instability of the FCU Flat Frames

The stability of the flat frames is an issue that should be investigated for creating accurate flat frames. The procedure described in Sec. 3.1 was repeated 10 times at each wavelength in the order of $7.7 \rightarrow 9.6 \rightarrow 11.5 \rightarrow 20.9 \rightarrow 7.7 \mu\text{m} \rightarrow \dots$ and so on. The average μ and the sample standard deviation σ of the flat values of 10 measurements were calculated for each pixel. Images of σ/μ were created, which are hereinafter called “temporal instability maps.”

4 Results

For the data obtained using the FCU, the count of a pixel was plotted against the average count in the photosensitive region in Fig. 5. The gradients were normalized such that the averages of the gradients in the photosensitive region were in unity. Figure 6 shows the resulting FCU flat frames compared with the conventional flat frames. Only the region where the detector was stable and suitable for evaluating the accuracy of flat frames is presented (see also Appendix A). The detector instability is a problem in photometry; however, we do not discuss this issue in depth because the main scope of this paper is to evaluate the accuracy of flat frames.

Figure 7 shows the flatness maps of the conventional flat-fielded images and those of the FCU flat-fielded images. Although the upper regions of the detector were dim in the conventional flat-fielded images, these patterns did not appear in the FCU flat-fielded images. In addition, the

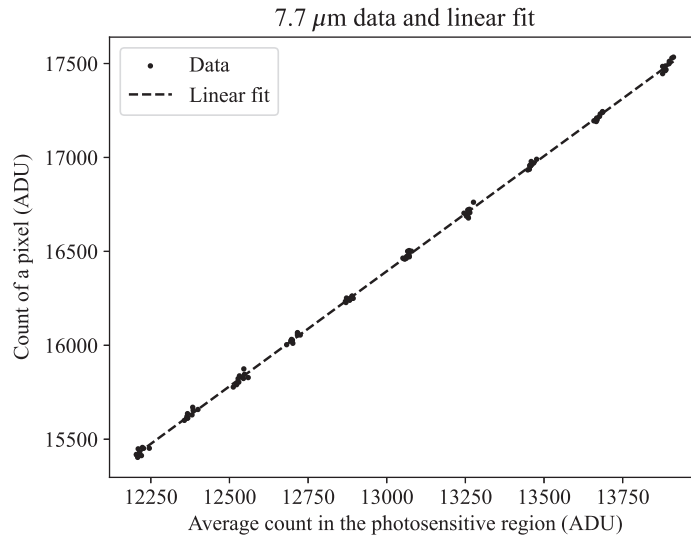


Fig. 5 Relationship between the measured count of a pixel and the average count in the photosensitive region, with a linear fit applied to them.

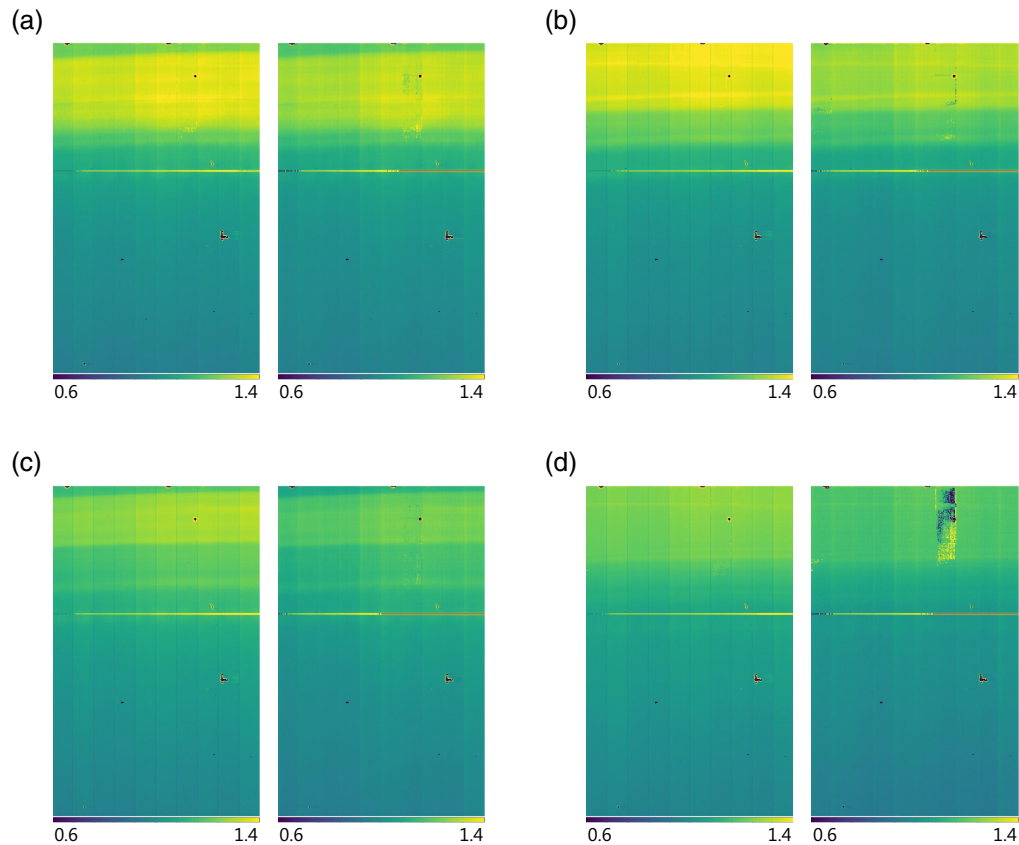


Fig. 6 Comparison between the conventional flat frame (left) and the FCU flat frame (right): (a) $7.7 \mu\text{m}$, (b) $9.6 \mu\text{m}$, (c) $11.5 \mu\text{m}$, and (d) $20.9 \mu\text{m}$. The bright horizontal bands in the upper region were caused by the MIMIZUKU optical system and may have resulted from multiple reflections in neutral-density filters used in the experiments. The horizontal lines located slightly above the middle are the rows of bad pixels. The rectangular region that shows different values from its surroundings, especially noticeable in the FCU flat frame at $20.9 \mu\text{m}$, is an area where the pixels are unstable.

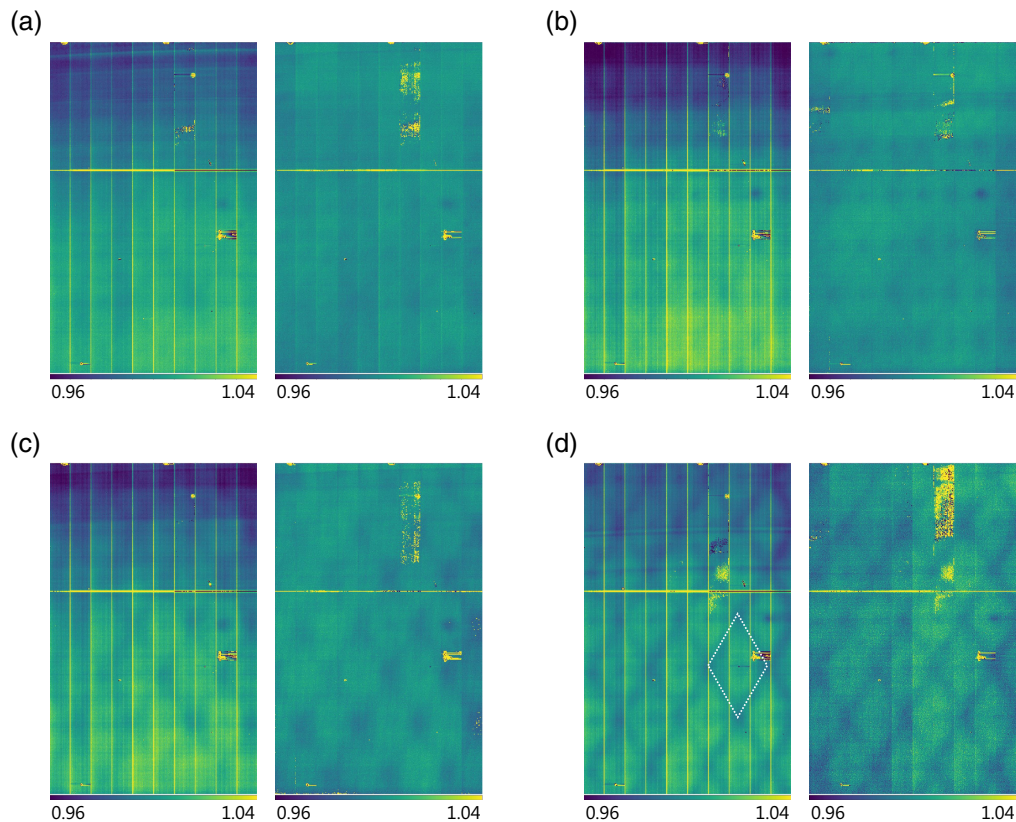


Fig. 7 Comparison between the flatness maps of the conventional flat-fielded image (left) and those of the FCU flat-fielded image (right): (a) $7.7 \mu\text{m}$, (b) $9.6 \mu\text{m}$, (c) $11.5 \mu\text{m}$, and (d) $20.9 \mu\text{m}$. The white dotted lines show the systematic diamond-shaped pattern derived from the reference images. Bad pixels are indicated by bright yellow or deep blue.

channel boundaries (vertical stripes) were bright in the conventional flat-fielded images, but these patterns did not appear in FCU flat-fielded images. The diamond-shaped patterns were observed in the flat-fielded images and were more pronounced at longer wavelengths. These patterns are not because of the flat frames but rather because of the reference images. Figure 8 shows the optical and thermal images of the blackbody. Distinct diamond-shaped patterns were observed and were responsible for the spatial non-uniformity in the surface brightness of the blackbody.

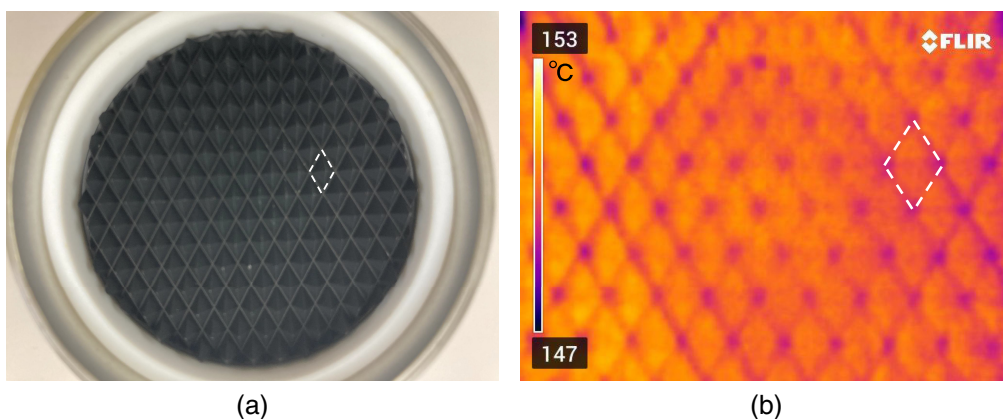


Fig. 8 Surface of the blackbody IRC 150 imaged by (a) a visible camera and (b) a thermal camera (FLIR C5, manufactured by FLIR). The white dashed lines indicate the diamond-shaped pattern that produced the non-uniformity of the surface brightness of the blackbody. The temperature scale on the left of the thermal image was derived assuming an emissivity of 0.98 for IRC 150.

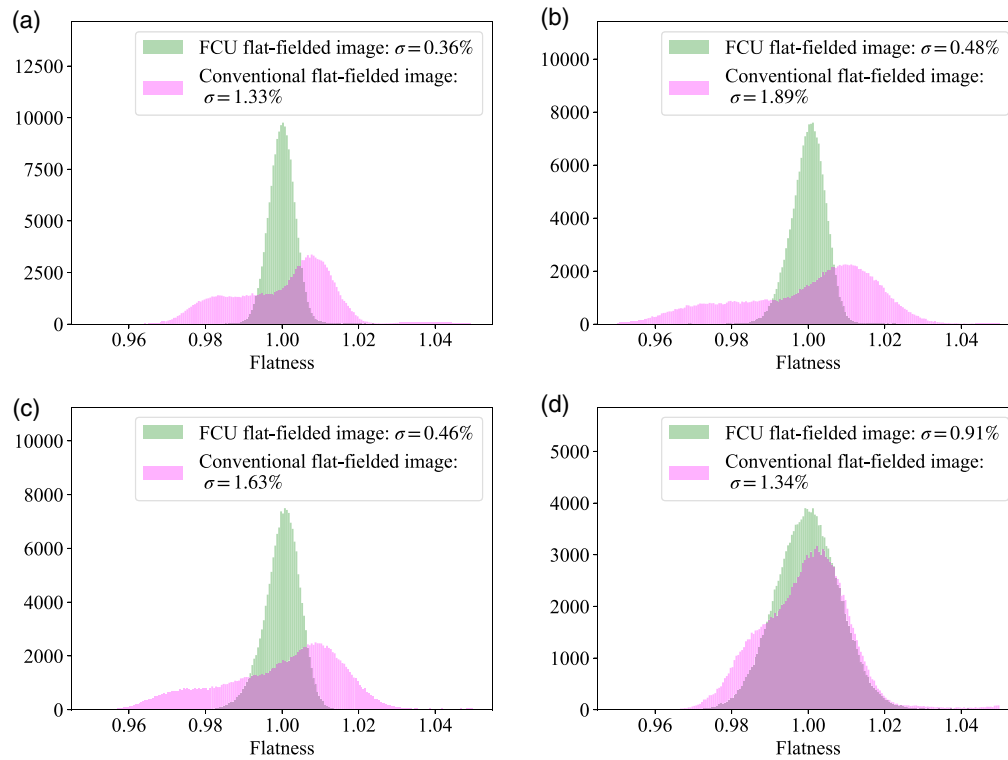


Fig. 9 Histograms of the flatness of the flat-fielded images (Fig. 7): (a) 7.7 μm , (b) 9.6 μm , (c) 11.5 μm , and (d) 20.9 μm . The green and magenta distributions represent the flatness of the FCU flat-fielded images and that of the conventional flat-fielded images, respectively. Their sample standard deviations are shown in the legend of each panel as σ derived after three-times 3-sigma clipping.

Figure 9 represents the histograms of the flatness maps of the flat-fielded images. The distributions were sharper for the FCU flat-fielded images than for the conventional flat-fielded images. In the FCU flat-fielded images, the sample standard deviation of the flatness, which is an indicator of the width of the distribution, was $\sim 1/4$ times at 7.7, 9.6, and 11.5 μm and was $\sim 2/3$ times at 20.9 μm compared with that of the conventional flat-fielded images. The wide distributions of the histograms for the conventional flat-fielded images were confirmed to be because of the gradation observed in Fig. 7 by creating the histograms of the upper and the lower half regions.

To investigate temporal instability, we visualized its spatial distribution and time-series variation. Figure 10 shows the temporal instability maps. Except for the specific unstable regions

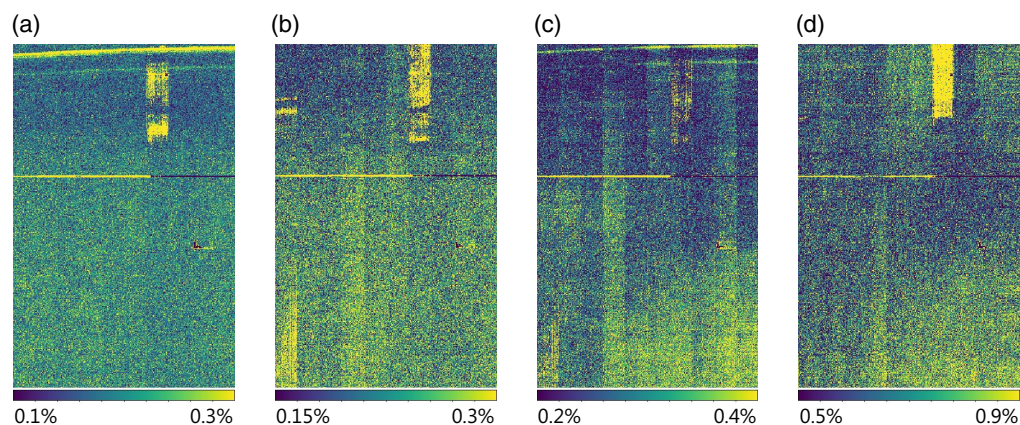


Fig. 10 Temporal instability map of the FCU flat frame: (a) 7.7 μm , (b) 9.6 μm , (c) 11.5 μm , and (d) 20.9 μm . Bad pixels are indicated by bright yellow or deep blue.

of certain unstable readout channels (e.g., the rectangular region in the top right part of the figure), there is no instability exceeding $\sim 1\%$. The entire region depicted in Fig. 10, excluding such unstable areas, was utilized for subsequent temporal analyses. Figure 11 indicates the time-series plots of flat values normalized along the time axis for each pixel. The flat values were generally stable at each wavelength but showed slight variations over long timescales at 11.5 and 20.9 μm . This suggests that the temporal instability of the flat values is caused by dominant random fluctuations and slight systematic variations.

We evaluated the accuracy of the FCU flat frames by measuring the flatness of the FCU flat-fielded images (Table 2). The flatness values were the standard deviations of the flatness maps, which excluded the three types of noise caused by the reference images. The first is random noise in the reference images, which was experimentally evaluated to be 0.037%, 0.049%, 0.049%, and 0.028% at 7.7, 9.6, 11.5, and 20.9 μm , respectively. The second is the non-uniformity of the blackbody surface temperature, which is 0.2 K in the specifications. In terms of intensity, this corresponds to a variation of 0.21%, 0.17%, 0.15%, and 0.096% at 7.7, 9.6, 11.5, and 20.9 μm , respectively. The third is attributed to the diamond-shaped patterns in the reference images. We modeled this component with a sine wave (Appendix B) and estimated its standard deviation to be 0.18%, 0.11%, 0.27%, and 0.34% at 7.7, 9.6, 11.5, and 20.9 μm , respectively.

The flatness represents the uncertainty of the flat frames and is considered to be contributed by the factors listed in the breakdown in Table 2. One is gradient uncertainty, which is due to stochastic variation in measured values (see Fig. 5). Another is temporal instability, which is caused by the difference in detector characteristics when creating the flat frames and when

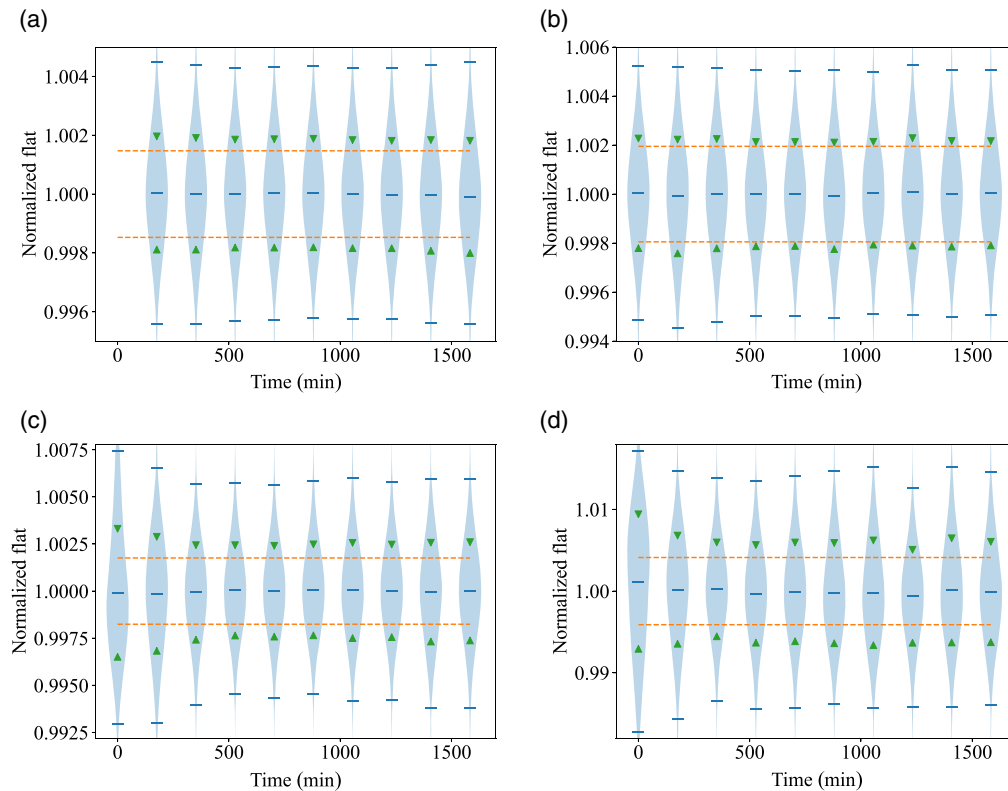


Fig. 11 Violin plots of the time-series data of normalized flat values: (a) 7.7 μm , (b) 9.6 μm , (c) 11.5 μm , and (d) 20.9 μm . The normalization of the flat values was conducted such that the average along the time axis for each pixel was in unity. The blue horizontal bars represent the top 1%, the mean, and the top 99% (bottom 1%) values at each measurement time in order from top to bottom. The green triangles represent the sample standard deviation from the mean of the data at each measurement time. All data contain the gradient uncertainties, whose $\pm 1\sigma$ are indicated by the orange horizontal dashed lines. The first data at 7.7 μm were excluded because the temperature of the blackbody was not sufficient.

Table 2 Flatness of the FCU flat-fielded images and its breakdown. The flatness is the sample standard deviations of the flatness maps shown in Fig. 9 excluding the uncertainties caused by the reference images. The gradient uncertainty was estimated from the propagation of the error assuming that the measured values follow the Gaussian distribution. Temporal instability was obtained by subtracting the contribution of gradient uncertainty from the average of the temporal instability map shown in Fig. 10. The residual uncertainty represents the uncertainty that is not attributed to either gradient uncertainty or temporal instability. The expected accuracy in aperture photometry is indicated in parentheses (see Sec. 5.5).

Wavelength (μm)	Flatness (%)	Breakdown		
		Gradient uncertainty (%)	Temporal instability (%)	Residual uncertainty (%)
7.7	0.23 (0.18)	0.15 (0.044)	0.13	0.12
9.6	0.43 (0.39)	0.19 (0.047)	0.12	0.37
11.5	0.34 (0.29)	0.18 (0.036)	0.22	0.20
20.9	0.84 (0.73)	0.41 (0.047)	0.52	0.51

creating the reference images. The residual uncertainty indicates the uncertainty that is not ascribed to either gradient uncertainty or temporal instability.

5 Discussion

5.1 Flatness

In this study, the flatness was improved qualitatively and quantitatively using the FCU. The dim patterns in the upper region in the conventional flat-fielded images disappeared in the FCU flat-fielded images. These patterns could have been created by the stable non-uniform irradiation from the entrance window or other parts. In the flat-fielding process using the FCU, this could have been successfully subtracted by extracting only the variable blackbody radiation from the FCU.

In addition, the bright patterns on the channel boundaries in the conventional flat-fielded images disappeared in the FCU flat-fielded images. These patterns could be attributed to the gain or offset of the detector. The gain and offset were defined as the gradient and vertical intercept of the response curve, respectively (see Fig. 1). The simplest explanation is that the gains of the boundaries were different from those of the other regions, and the differences were corrected well by the local gradient method using the FCU. Another possibility is that the offset varied with the irradiation level. It is difficult to determine whether the gain or the offset has changed. Whichever is correct, the reason for the better accuracy of the FCU flat frames is considered to be based on the local gradient method.

5.2 Gradient Uncertainty

Gradient uncertainty was a little lower than 0.2% at 7.7, 9.6, and 11.5 μm and $\sim 0.4\%$ at 20.9 μm . These uncertainties are limited by the number of images acquired to create flat frames and would be improved by taking more images. Although the number of images to create flat frames was the same for all four wavelengths, the gradient uncertainty at 20.9 μm was approximately twice as large as that at the other wavelengths. This is due to the narrow count range used in the least-square fitting for the data at 20.9 μm : a count range of 13,000 to 14,000 ADU was used for 20.9 μm , whereas that of 12,000 to 14,000 ADU was used for the other wavelengths (see Appendix C for details).

The problem of the narrow count range at 20.9 μm could be improved by increasing the contribution of the blackbody radiation to the room temperature radiation, for example, using a blackbody with a higher maximum temperature. To double the contribution of the blackbody radiation, the maximum temperature of the blackbody should be raised from 150°C to 350°C. Another solution would be to use an integrating sphere to increase the intensity of the blackbody radiation.

The photometric error due to the gradient uncertainty is expected to be lower than the gradient uncertainty itself by approximately one order of magnitude in aperture photometry (see Table 2 and Sec. 5.5). Even without this improvement, the measured flatness was better than 1%, demonstrating that flat fielding using the FCU is effective for achieving 1% photometric accuracy.

5.3 Temporal Instability

First, we discuss the spatial structure of temporal instability maps. Figure 10 shows that the lower right region was unstable for longer wavelengths. This region is strongly affected by the absorption of the lens because the light reaching this region passes through the thick region of the lens (see Appendix A). Therefore, the variation in the absorption coefficients might contribute to temporal instability. A previous study reported that the transmittance of silicon is dependent on the temperature,²¹ and the measured temporal instability of the flat frames is consistent with a temperature fluctuation in the order of 1 K, which is derived from Fig. 1-25 in Ref. 21. By monitoring the temperature, it may be possible to estimate the temperature dependence of the absorption coefficients experimentally.

Next, we discuss the time-series variation of the flat values. Figure 11 shows that the flat values generally varied randomly, suggesting that the amplifiers of individual detector pixels changed separately because there was little correlation between pixels. On the contrary, the flat values show slight systematic variations at 11.5 and 20.9 μm . This suggests the influence of time variation of lens absorption already discussed in the previous paragraph. Overall, however, the flat values are stable over 29 h, and it is sufficient to obtain flat frames once per night.

5.4 Residual Uncertainty

There was uncertainty that was not attributed to either gradient uncertainty or temporal instability. The residual uncertainty included the following two uncertainties: one was the uncertainty of the correction of absorption and reflection described in Appendix A. Its contribution is difficult to estimate because the true patterns created by absorption and reflection are unknown. The other was the uncertainty caused by channel instability, which is the temporal fluctuation of the offsets of the detector channels. Its contribution may have a major influence as significant as the diamond-shaped patterns (see Fig. 15 in Appendix B for details). It is more pronounced at 9.6 and 20.9 μm , which is consistent with the tendency for the residual uncertainty to be large at these wavelengths. Additional confirmation is required, but the latter factor may determine the limit of the accuracy of our correction method for the optical system.

5.5 Prediction of Photometric Accuracy in Aperture Photometry

We discussed the accuracy of flat frames for individual detector pixels. However, the random uncertainty decreases in aperture photometry as multiple pixels were used. Assuming the point spread function (PSF) was the Airy pattern in the diffraction limit, the aperture diameters defined by three times the full-width at half-maximum (FWHM) of the PSF were 6.9, 8.6, 10.3, and 18.7 pixels at 7.7, 9.6, 11.5, and 20.9 μm , respectively. Considering the contribution of each pixel to aperture photometry, the random uncertainties in aperture photometry were expected to be 0.30, 0.24, 0.20, and 0.11 times the value for one pixel at 7.7, 9.6, 11.5, and 20.9 μm , respectively.

It was difficult to determine the extent to which the temporal instability and residual uncertainty were random. However, the gradient uncertainty is considered random. By multiplying the values listed in Table 2 by the factor mentioned in the previous paragraph, we obtained the photometric accuracy originating from the gradient uncertainty to be 0.044%, 0.047%, 0.036%, and 0.047% at 7.7, 9.6, 11.5, and 20.9 μm , respectively. By replacing the gradient uncertainty in Table 2 with these values, the photometric accuracy with the use of the FCU was calculated to be 0.18%, 0.39%, 0.29%, and 0.73% at 7.7, 9.6, 11.5, and 20.9 μm , respectively. These values are listed in Table 2 in parentheses. This demonstrates that the FCU we developed in this study is capable of achieving 1% photometric accuracy.

In this study, we did not assess the influence of the folding mirrors on flat fielding. The properties of the folding mirrors, such as the reflectance non-uniformity and the polarization-direction dependence of reflectance, can cause systematic patterns in flat frames. If we find

that the folding mirrors have a significant impact, we are considering eliminating this effect by correcting the pattern derived from the mirrors. We would obtain the pattern by dividing the flat frames acquired with the folding mirrors by those acquired without them. The photometric accuracy, including the correction for atmospheric absorption using the FS, will be evaluated in the actual observations of TAO/MIMIZUKU.

6 Conclusions

In this study, we developed an FCU to perform flat fielding with an accuracy of better than 1% in the MIR region. The proof-of-concept tests evaluating the accuracy and stability of the flat frames obtained using the FCU demonstrated as follows.

1. Visually better images were produced by the FCU flat frames than by conventional flat frames.
2. Quantitatively, the uncertainty of the FCU flat frames was approximately one-fourths at 7.7, 9.6, and 11.5 μm and two-thirds at 20.9 μm compared with that of conventional flat frames.
3. The photometric accuracy in aperture photometry was predicted to be 0.18%, 0.39%, 0.29%, and 0.73% at 7.7, 9.6, 11.5, and 20.9 μm , respectively.
4. The FCU flat frames have remained stable over a period of 29 h. Thus it is sufficient to acquire flat frames once per night.

Overall, the accuracy of the FCU flat frames has reached a sufficient level to achieve our goal of 1% monitoring photometric accuracy. This will enable us to explore time-domain astronomy in the MIR region, which is expected to yield essentially new information that would not be obtainable in a snapshot.

7 Appendix A: Correction of Absorption and Reflection Caused by the Silicon Lens

Ideally, the FCU should irradiate the detector uniformly with an accuracy of much better than 1%. However, practically, concentric patterns appeared in the reference images divided by the FCU flat frames, as shown in Fig. 12(a). There were typically 2% offsets between the regions with different readout channels. They were corrected in Fig. 12 for visibility but not in the other analyses.

These concentric patterns were explained as a combination of light passing through the lens without reflection and the light reflected twice at the surfaces of the lens [i.e., one round-trip in the lens, see Fig. 13(a)]. They were modeled by the following equations:

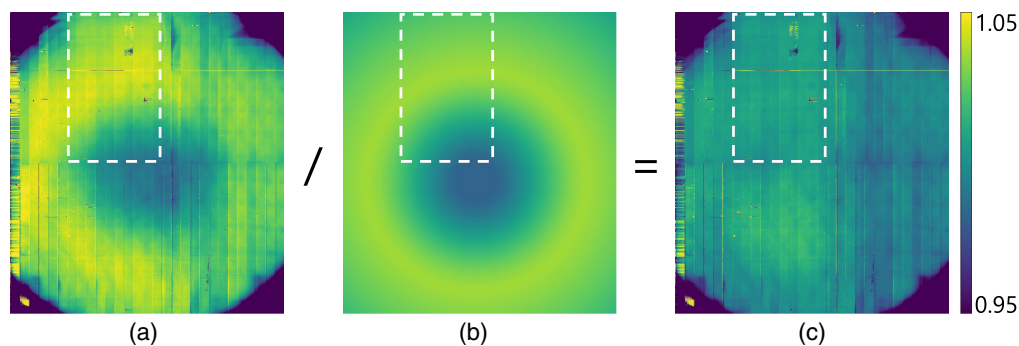


Fig. 12 (a) Reference image divided by the FCU flat frame at 7.7 μm (before correction). The concentric pattern appeared because flat frames were affected by the absorption and reflection of the silicon lens. Offsets between the regions with different readout channels were corrected for visibility. (b) Correction map derived from Eq. (4) (absorption and reflection pattern). (c) Reference image divided by the FCU flat frame after correction. The concentric pattern was canceled out. In the main analyses, only the region enclosed by the white dashed line was used because the other region is not suitable for evaluating the accuracy of flat frames due to high detector instability, which includes both temporal instability and bad outputs.

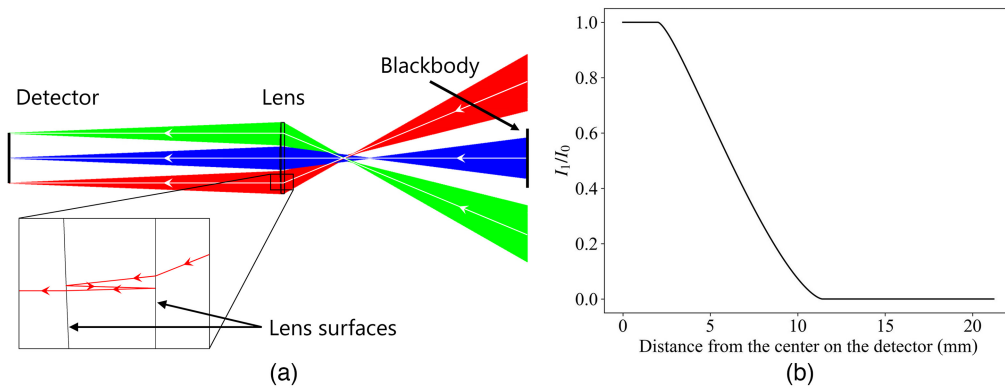


Fig. 13 (a) Path of the light reflected twice at the lens surfaces. The arrows indicate the direction of light propagation. The light incident on the center of the detector (depicted in blue) is emitted from the blackbody. The blackbody contribution decreases as the distance increases from the center; finally, it reaches zero (depicted in green and red). (b) Dependency of I_1/I_0 on the location on the detector coordinates. The I_0 and I_1 are the intensity of the incident blackbody radiation of the unreflected and that of one round-trip, respectively.

$$I_T = I_0(1 - R)^2 \exp(-at) + I_1(1 - R)^2 R^2 \exp(-3at), \quad (3)$$

$$= I_0(1 - R)^2 \left[\exp(-at) + \frac{I_1}{I_0} R^2 \exp(-3at) \right], \quad (4)$$

where I_T , I_0 , and I_1 are the total intensity of the blackbody radiation reaching the detector, incident intensity of the blackbody radiation without reflection, and incident intensity of the

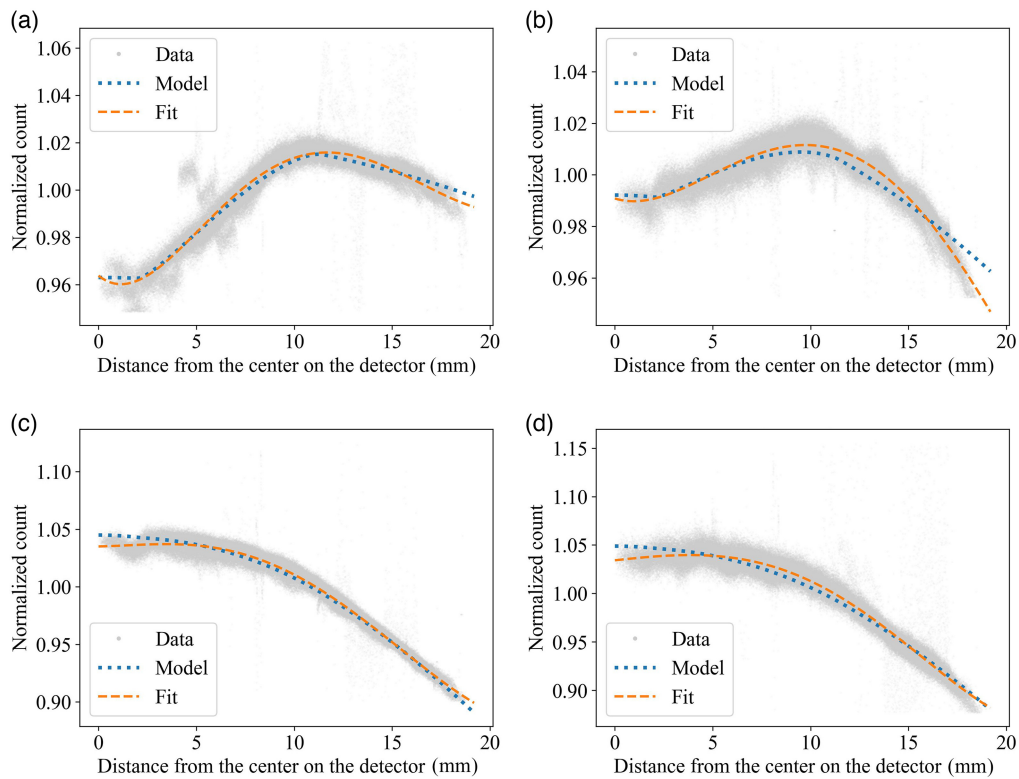


Fig. 14 Radial distributions of the counts in the reference image after being divided by the FCU flat frame: (a) $7.7 \mu\text{m}$, (b) $9.6 \mu\text{m}$, (c) $11.5 \mu\text{m}$, and (d) $20.9 \mu\text{m}$. The 3-sigma clipping was applied three times. The blue dotted curves represent the model curves based on Eq. (4). The orange dashed curves, which are the fifth-order polynomial fits to the data, are used instead of model curves.

blackbody radiation with one round-trip path in the lens, respectively (their dimensions are $\text{W m}^{-2} \text{str}^{-1}$). The α is the absorption coefficient of the silicon lens, t is the lens thickness, and R is the silicon reflectance. I_1 depends on the location on the detector, as shown in Fig. 13(a). Figure 13(b) shows the location dependence of I_1/I_0 calculated from the optical model. The contribution of blackbody radiation decreases with increasing distance from the center. We adopted $R = 0.3$, which is the typical value of the silicon reflectance in the N and Q bands.²² In this case, the light that makes more than two round-trips in the lens was ignored because it contributed to $<0.1\%$ to the total intensity. To reproduce the data, we adopted $\alpha = 0.04, 0.10, 0.25,$ and 0.27 mm^{-1} at $7.7, 9.6, 11.5,$ and $20.9 \mu\text{m}$, respectively.

This model reproduced the measured patterns well, as demonstrated in Figs. 12 and 14. However, the data show features that could not be fully explained by the model. Hence, we adopted a fifth-order polynomial fit. The fitting parameters were the coefficients of the polynomial and the center position of the concentric patterns on the detector coordinates. The best values of the parameters were determined by minimizing the residual sum of squares between the fit and data.

8 Appendix B: Evaluation of Uncertainty Caused by the Diamond-Shaped Patterns

To assess the uncertainty caused by the diamond-shaped patterns, we modeled the horizontal cross-section profile of the patterns using a sine wave:

$$f(x) = A \sin(kx - \phi) + f_0, \quad (5)$$

where $A, k, \phi,$ and f_0 are the fitting parameters. The best-fit models are shown in Fig. 15.

Generally, the standard deviation σ of a physical quantity following a periodic function $f(x)$ is given by

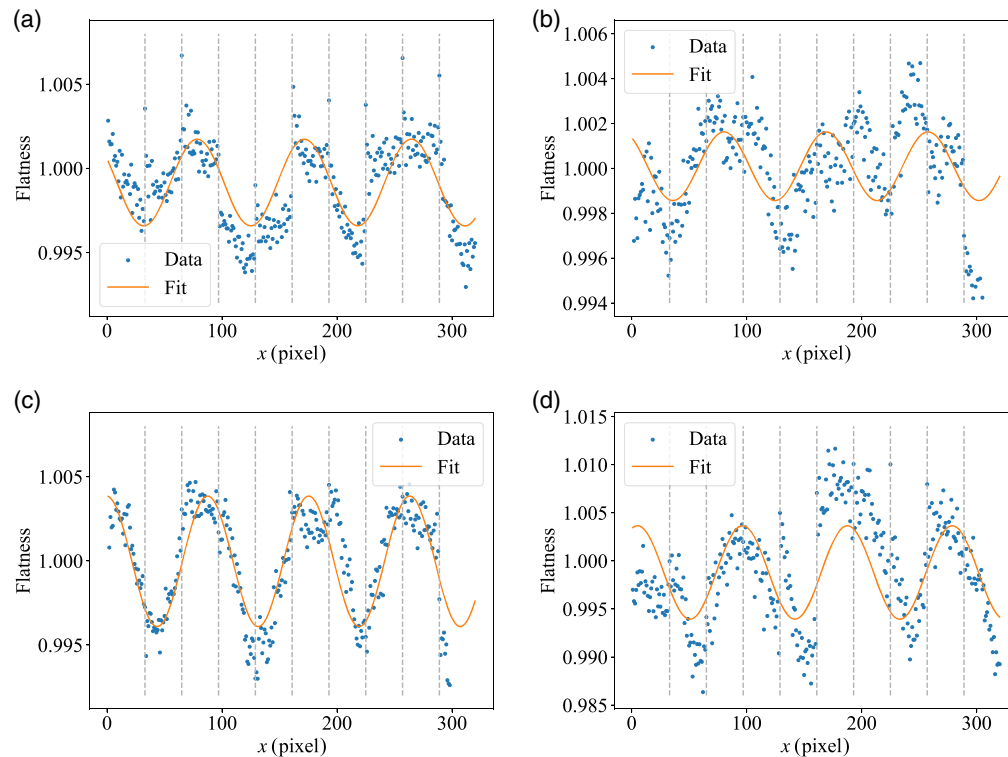


Fig. 15 Horizontal cross section of the flatness maps: (a) $7.7 \mu\text{m}$, (b) $9.6 \mu\text{m}$, (c) $11.5 \mu\text{m}$, and (d) $20.9 \mu\text{m}$. The data are plotted as blue dots, and the best-fit models are shown as orange solid curves. The gray dashed lines represent the boundaries of the detector channels. The data of several channels exhibit offsets in addition to the sinusoidal trends.

$$\sigma = \sqrt{\frac{1}{P} \int_{x_0}^{x_0+P} (f(x) - \mu)^2 dx} = \sqrt{\frac{1}{P} \int_{x_0}^{x_0+P} (f(x))^2 dx} - \mu^2, \quad (6)$$

where P and μ are the period and mean of $f(x)$, respectively. Substituting Eq. (5) into Eq. (6), we obtain $\sigma = A/\sqrt{2}$.

9 Appendix C: Mathematical Interpretation of Gradient Uncertainty

We considered the relative uncertainty of the gradients obtained using the least-squares method. We defined x_i as the average count of each frame, y_i as the count of a pixel, N as the number of the obtained data, a as the gradient acquired using the least-squares method, and σ_a as the uncertainty of a . The y_i was assumed to be distributed according to Gaussian distribution with a standard deviation of σ_y . The a and σ_a are given by the following equations:

$$a = \frac{N \sum_i x_i y_i - \sum_i x_i \sum_i y_i}{N \sum_i x_i^2 - \left(\sum_i x_i \right)^2}, \quad (7)$$

$$\sigma_a = \frac{1}{\sqrt{N}} \frac{\sigma_y}{\sqrt{\sum_i x_i^2 / N - \left(\sum_i x_i / N \right)^2}} = : \frac{1}{\sqrt{N}} \sigma_x \left(\sigma_y = \sqrt{\frac{1}{N-2} \sum_i [y_i - (ax_i + b_i)]^2} \right), \quad (8)$$

where σ_x is the standard deviation of x_i . Although we are interested in the relative uncertainty σ_a/a , it is sufficient to consider σ_a because a does not strongly depend on the number of data. As the number of data N increases, σ_y is invariant according to the definition, and σ_x changes little if the count range remains the same. Therefore, σ_a is almost proportional to $1/\sqrt{N}$. When the data are taken at equal intervals, σ_x is proportional to the count range. At $20.9 \mu\text{m}$, the count range was approximately half that at the other wavelengths; thus σ_a is approximately twice as large.

Code, Data, and Materials Availability

The data that support the findings of this article are not publicly available. They can be requested from the author at naruse-akira151@g.ecc.u-tokyo.ac.jp.

Acknowledgments

This research and its development were supported by JSPS Grant-in-Aid for Scientific Research B (Grant No. JP20H01943) and JSPS Grant-in-Aid for Scientific Research on Innovative Areas (Grant No. JP18H05440). We are grateful to the referees for useful comments. There are no potential conflicts of interest to disclose. This paper is based on an advanced version of the study reported in Ref. 23.

References

1. D. Charbonneau et al., “Detection of planetary transits across a sun-like star,” *Astrophys. J.* **529**, L45–L48 (2000).
2. W. J. Borucki et al., “Kepler planet-detection mission: introduction and first results,” *Science* **327**, 977 (2010).
3. G. R. Ricker et al., “Transiting Exoplanet Survey Satellite (TESS),” *J. Astron. Telesc. Instrum. Syst.* **1**, 014003 (2015).
4. M. A. Thompson et al., “Studying the evolution of warm dust encircling BD +20 307 using SOFIA,” *Astrophys. J.* **875**, 45–53 (2019).
5. T. Miyata et al., “Development of a new mid-infrared instrument for the TAO 6.5-m telescope,” *Proc. SPIE* **7735**, 77353P (2010).
6. T. Kamizuka et al., “Development of MIMIZUKU: a mid-infrared multi-field imager for 6.5-m TAO telescope,” *Proc. SPIE* **8446**, 84466P (2012).
7. T. Kamizuka et al., “Revised specifications and current development status of MIMIZUKU: the mid-infrared instrument for the TAO 6.5-m telescope,” *Proc. SPIE* **9147**, 91473C (2014).
8. T. Kamizuka et al., “Development status of the mid-infrared two-field camera and spectrograph MIMIZUKU for the TAO 6.5-m Telescope,” *Proc. SPIE* **9908**, 99083W (2016).

9. T. Kamizuka et al., “Laboratory performance evaluation of the mid-infrared camera and spectrograph MIMIZUKU for the TAO 6.5-m telescope,” *Proc. SPIE* **10702**, 107022H (2018).
10. T. Kamizuka et al., “The University of Tokyo Atacama Observatory 6.5 m telescope: on-sky performance evaluations of the mid-infrared instrument MIMIZUKU on the Subaru telescope,” *Proc. SPIE* **11447**, 114475X (2020).
11. Y. Yoshii et al., “Tokyo atacama observatory project,” in *8th Asian-Pac. Regional Meet.*, S. Ikeuchi, J. Hearnshaw, and T. Hanawa, Eds., Proceedings of the IAU 8th Asian-Pacific Regional Meeting, Vol. II, pp. 35–36 (2002).
12. Y. Yoshii et al., “The University of Tokyo Atacama Observatory 6.5 m telescope project,” *Proc. SPIE* **7733**, 773308 (2010).
13. Y. Yoshii et al., “Overview of University of Tokyo Atacama Observatory 6.5 m telescope project,” *Proc. SPIE* **9145**, 914507 (2014).
14. Y. Yoshii et al., “The University of Tokyo Atacama Observatory 6.5 m telescope: project overview and current status,” *Proc. SPIE* **9906**, 99060R (2016).
15. M. Doi et al., “The University of Tokyo Atacama Observatory 6.5 m telescope: project overview and current status,” *Proc. SPIE* **10700**, 107000W (2018).
16. M. S. Uchiyama et al., “Development of an optical device (Field Stacker) for achieving accurate photometry in ground-based mid-infrared observations,” *Proc. SPIE* **9912**, 99125N (2016).
17. The Past and Current Members of the COMICS Team and Subaru Telescope, *Subaru Data Reduction Cookbook: COMICS*, Subaru Telescope, Version. 2.1.2e ed. (2012).
18. A. J. Claret et al., “Calibration of VISIR: the VLT mid-infrared imager/spectrometer,” *Proc. SPIE* **4841**, 252–262 (2003).
19. C. Telesco et al., *CanariCam Astronomers User Manual*, Gran Telescopio Canarias, Version 1.3 ed. (2009).
20. T. Michifuji et al., “Development of flat fielding method in MIR for accurate photometry with TAO/MIMIZUKU,” *Proc. SPIE* **11447**, 114479M (2020).
21. G. J. Hawkins, “Spectral characterisation of infrared optical materials and filters,” PhD thesis, University of Reading (1998).
22. D. F. Edwards and E. Ochoa, “Infrared refractive index of silicon,” *Appl. Opt.* **19**, 4130–4131 (1980).
23. A. C. Naruse et al., “Development of a flat calibration unit for TAO/MIMIZUKU,” *Proc. SPIE* **12188**, 121883U (2022).

Biographies of the authors are not available.